Research Article

Nano Research
2022, 15(7): 6156–6167

ISSN 1998-0124 CN 11-5974/O4
https://doi.org/10.1007/s12274-022-4242-5

Liquid-phase sintering enabling mixed ionic-electronic interphases and free-standing composite cathode architecture toward high energy solid-state battery

Xiang Han[1], Weijun Zhou[1], Minfeng Chen[1], Linshan Luo[2], Lanhui Gu[1], Qiaobao Zhang[4], Jizhang Chen[1] (✉), Bo Liu[3] (✉), Songyan Chen[2] (✉), and Wenqing Zhang[5]

[1] College of Materials Science and Engineering, Nanjing Forestry University, Nanjing 210037, China
[2] Department of Physics, Xiamen University, Xiamen 361005, China
[3] College of Mathematics and Physics, Jinggangshan University, Ji'an 343009, China
[4] Department of Materials Science and Engineering, College of Materials, Xiamen 361005, China
[5] Department of Physics, Southern University of Science and Technology, Shenzhen 518055, China

Received: 23 December 2021 / **Revised:** 24 January 2022 / **Accepted:** 15 February 2022

ABSTRACT

Solid-state batteries (SSBs) will potentially offer increased energy density and, more importantly, improved safety for next generation lithium-ion (Li-ion) batteries. One enabling technology is solid-state composite cathodes with high operating voltage and area capacity. Current composite cathode manufacturing technologies, however, suffer from large interfacial resistance and low active mass loading that with excessive amounts of polymer electrolytes and conductive additives. Here, we report a liquid-phase sintering technology that offers mixed ionic-electronic interphases and free-standing electrode architecture design, which eventually contribute to high area capacity. A small amount (~ 4 wt.%) of lithium hydroxide (LiOH) and boric acid (H_3BO_3) with low melting point are utilized as sintering additives that infiltrate into single-crystal Ni-rich $LiNi_{0.8}Mn_{0.1}Co_{0.1}$ (NMC811) particles at a moderately elevated temperature (~ 350 °C) in a liquid state, which not only enable intimate physical contact but also promote the densification process. In addition, the liquid-phase additives react and transform to ionic-conductive lithium boron oxide, together with the indium tin oxide (ITO) nanoparticle coating, mixed ionic-electronic interphases of composite cathode are successfully fabricated. Furthermore, the liquid-phase sintering performed at high-temperature (~ 800 °C) also enables the fabrication of highly dense and thick composite cathodes with a novel free-standing architecture. The promising performance characteristics of such composite cathodes, for example, delivering an area capacity above 8 mAh·cm^{-2} within a wide voltage window up to 4.4 V, open new opportunities for SSBs with a high energy density of 500 Wh·kg^{-1} for safer portable electronic and electrical transport.

KEYWORDS

solid-state battery, single-crystal Ni-rich $LiNi_{0.8}Mn_{0.1}Co_{0.1}$, liquid-phase sintering, mixed ionic-electronic interphases, free-standing architecture

1 Introduction

Rechargeable solid-state batteries (SSBs) have been widely explored in the hope of increasing the specific energy and, most importantly, resolving the safety issues of lithium-ion (Li-ion) batteries for zero-emission electric vehicles and clean energy storage technologies [1–6]. Li metal, with high theoretical capacity and low redox potential, is promising for utilization in SSBs because solid-state electrolytes (SSEs) commonly offer better resistance to Li dendrite penetration for improved Li metal battery durability and safety [7–11]. For a solid-state Li metal battery, the specific energy density is determined by the electrochemical characteristics of the cathode side and SSE, such as a high specific capacity and high-voltage cathode material as well as a thin but highly ionic conductive SSE film [12, 13]. Among various cathode materials, Ni-rich layered oxide materials are very attractive because of their high specific capacity, high operating voltage, and low cost [14–18]. In addition, it has been demonstrated that single-crystal layered oxide cathodes exhibit good cycling stability and rate performance in SSBs, among others [19–22]. For a practical pouch-type solid-state cell design, it has been calculated that a cathode loading of at least 5 mAh·cm^{-2} is essential to achieve a 500 Wh·kg^{-1} SSB [23]. Considering that the area capacity is highly dependent on the specific capacity and mass loading, one should aim to prepare a high-loading composite cathode with mixed ionic-electronic conductive interphases, which is normally needed for a high-energy-density SSB.

Currently explored composite cathode manufacturing technologies, however, fail to even match the volumetric performance characteristics of commercial high-energy cells (e.g., 3 mAh·cm^{-2}) [24–28]. The reason is that the traditional fabrication method is typically based on the traditional slurry casting electrode fabrication technique except for introducing polymer electrolytes

Address correspondence to Jizhang Chen, chenjizhang@njfu.edu.cn; Bo Liu, liubo@jgsu.edu.cn; Songyan Chen, sychen@xmu.edu.cn

or ionic liquids to wet the interfaces between cathode active materials and ceramic SSEs. In composite electrodes, large volume fractions of ceramic SSE powders or polymer electrolytes are typically required to ensure that all active particles are uniformly surrounded due to the high hardness of layered oxide cathodes. The large amount of porous polymer electrolyte reduces the density of the cathode but also induces large interfacial resistance due to its intrinsic low ionic conductivity.

Designing three-dimensional (3D) ionic conducting scaffolds [29, 30] and *in-situ* polymerization techniques [31] have been demonstrated to reduce the interfacial resistance between cathode active material and SSE. Another strategy is co-sintering active cathode materials and ceramic SSEs on dense SSE pellets with the assistance of low-melting point additives, which involves separate and slow fabrications of dense sintered SSE pellets and then sintered composite electrodes together. Li_3BO_3, B_2O_3, and $Li_{2.3}C_{0.7}B_{0.3}O_3$ sintering additives have been explored [32–34], which not only serve as a solder that binds active materials but also facilitate interfacial Li-ion transport. However, because ceramic is brittle and contains defects that may induce cracking under stress during cell assembly, SSE membranes are typically relatively thick (> 100 μm, an order of magnitude thicker than the porous polymer membranes used in commercial Li-ion cells), which takes extra space and mass [32–35]. Additionally, the high melting point of the explored ceramic SSEs in combination with their poor contact on the surface of active materials often requires high pressure and temperature (> 600 °C), which cause serious side reactions that lead to high interfacial resistance and low capacity [36]. Very recently, to overcome the limitations of conventional co-sintering manufacturing, solution infiltration of anti-perovskite SSEs $Li_{2.985}B_{0.005}OCl$ and $Li_{1.9}OHCl_{0.9}$ into regular electrodes was proposed at a low temperature of 300 °C [37, 38], which is also compatible with traditional electrode winding technology. Unfortunately, the air-sensitive nature of $Li_{1.9}OHCl_{0.9}$ and operation in a moisture-free environment limit the scalability of such a process.

In this work, with single-crystal $LiNi_{0.8}Mn_{0.1}Co_{0.1}$ (NMC811) as the starting material, we used low-melting-point lithium hydroxide (LiOH) and boric acid (H_3BO_3) composite additives that show a low surface energy of 55 $mJ \cdot m^{-2}$ and good wettability against cathode materials. Additionally, indium tin oxide (ITO) nanoparticles were coated on the surface of NMC811, which not only improve the electrical conductivity to establish an interfacial electron pathway but also increase the surface energy of NMC811 that further promote the densification process. Consequently, as shown in Fig. 1(a), scalable manufacturing of the NMC811 composite cathode is enabled on Al foil, the process of which involved infiltration of the composite additive into dense, thermally stable electrodes at moderate temperatures (~ 350 °C) in a liquid state and then solidification during cooling. During this melting infiltration process, the additive converts to $Li_2B_4O_7$ and $LiBO_2$ composite (denoted as LBO_x). The *in-situ* formed LBO_x interphases not only enhance interfacial mechanical adhesion but also facilitate lithium Li^+ ion transport. Meanwhile, the electrically conductive ITO coating helps to build a fast electron pathway between the well-connected NMC811 particles. The self-interconnected and monothetic NMC811/LBO_x/ITO cathode with mixed ionic-electronic conductive interphases, which is normally needed for the electrochemical reaction to occur, exhibited a high specific capacity of 207 $mAh \cdot g^{-1}$, good rate capability, and excellent capacity retention during long-term testing. At an elevated temperature of ~ 800 °C, as shown in Fig. 1(b), the liquid-phase sintering process technique further promotes the densification process and enables us to fabricate free-standing and densely packed NMC811/$LiBO_x$/ITO composite cathodes. The compact and thick NMC811/LBO_x/ITO composite cathode shows not only high density (4.3 $g \cdot cm^{-3}$) but also high conductivity (0.94×10^{-3} $S \cdot cm^{-1}$). Tested in a solid-state cell, a superior high area capacity of up to 8 $mAh \cdot cm^{-2}$ was achieved, exhibiting great promise toward realization of a 500 $Wh \cdot kg^{-1}$ SSB.

2 Experimental section

2.1 Materials synthesis

NASICON-type $Li_{1.3}Al_{0.3}Ti_{1.7}(PO_4)_3$ (LATP) was synthesized by a

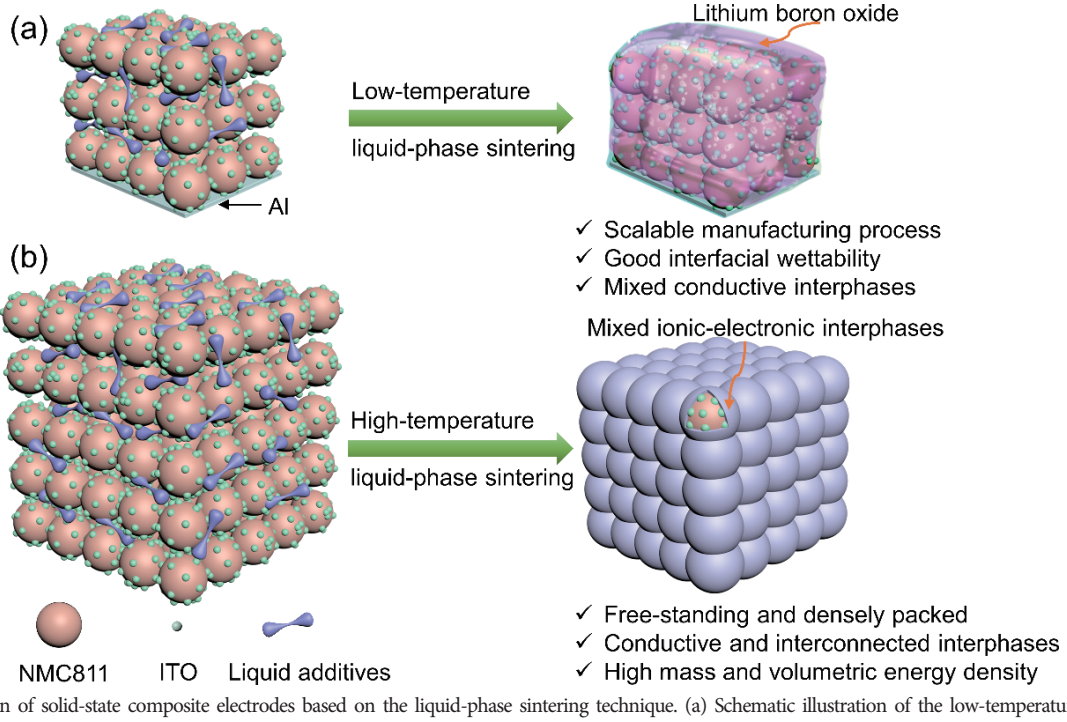

Figure 1 Design of solid-state composite electrodes based on the liquid-phase sintering technique. (a) Schematic illustration of the low-temperature liquid-phase sintering for scalable fabrication of the NMC811/LBO_x/ITO composite cathode on Al foil and its advantages. (b) Schematic illustration of high-temperature liquid-phase sintering of a thick and densely packed NMC811/LBO_x/ITO composite cathode and its advantages.

solid-state reaction method. The starting materials were $LiOH{\cdot}H_2O$ (99.95%, Sigma Aldrich), Al_2O_3 (99.99%, Sigma Aldrich), TiO_2 (99.8%, Sigma Aldrich), and $NH_4H_2PO_4$ (99.5%, Sigma Aldrich) powders. $LiOH{\cdot}H_2O$ was heated at 250 °C for 3 h to remove crystalline H_2O prior to use. Stoichiometric amounts of chemicals with 10 wt.% excess LiOH were hand-ground for 0.5 h in an agate mortar. The mixed powders were then cold pressed into pellets with diameters of 13 mm at 400 MPa. Next, the pellets were preheated at 400 °C in air for 3 h, hand-ground into fine powders, cold-pressed into pellets and sintered at 900 °C for 5 h. The synthesized LATP pellet was ball milled (600 r·min^{-1} for 5 h) into fine nanoparticles.

LCO/LiBO$_x$/ITO composite cathode on Al foil. Raw layered transition metal oxide $LiCoO_2$ (LCO) particles (94 wt.%), LiOH + H_3BO_3 (4 wt.%, Li/B molar ratio is 1), and ITO (2 wt.%) powders were mixed in an agate mortar for 0.5 h. Then, the mixed powders were milled with 5 wt.% polyvinylidene fluoride (PVDF) (dissolved in N-methyl-2-pyrrolidone (NMP)) to make a slurry. The as-obtained slurry was cast on carbon-coated Al foil. After vacuum drying at 80 °C for 2 h, the electrode was cut into small disks with a diameter of 12 mm. Then, the electrodes were transferred into a tube furnace and heat-treated for 1 h at 300 °C under high-purity Ar (99.999%) flow. The elevated temperature rate was 5 °C·min^{-1}, and the electrodes were cooled naturally. The LCO active material loading was 6–8 mg·cm^{-2}.

NMC811/LiBO$_x$/ITO composite cathode on Al foil. Raw NMC811 particles (94 wt.%), LiOH + H_3BO_3 (4 wt.%, Li/B molar ratio of 1), and ITO (2 wt.%) powders were mixed in an agate mortar for 0.5 h. Then, the mixed powders (400 mg) were milled with PVDF (20 mg, dissolved in NMP) to make a slurry. The as-obtained slurry was cast on carbon-coated Al foil. After vacuum drying at 80 °C for 2 h, the electrode was cut into small disks with a diameter of 12 mm, followed by cold pressing under 300 MPa for 5 min. Then, the small disk electrodes were transferred into a tube furnace and heat-treated for 1 h at 300 °C under high-purity Ar (99.999%) flow, with a heating rate of 5 °C·min^{-1}, and cooled naturally. The as-obtained NMC811/LiBO$_x$/ITO composite electrodes were directly transferred into an Ar-filled gloved box for battery assembly. The NMC811 active material loading was 6–8 mg·cm^{-2}.

Free-standing and thick NMC811/LiBO$_x$/ITO composite cathode. Raw NMC811 particles (94 wt.%), LiOH + H_3BO_3 (4 wt.%, Li/B molar ratio of 1), and ITO (2 wt.%) powders were mixed in an agate mortar for 0.5 h and then cold pressed at 300 MPa for 10 min in a die with a diameter of 12 mm. The as-obtained pellet was then transferred into a tube furnace and heated at 800 °C for 2 h under pure O_2 (99.999%) flow. The obtained thick NMC811/LiBO$_x$/ITO pellet was polished and ultrasonically cleaned in EtOH three times. The thickness of the NMC811/LiBO$_x$/ITO pellet was ~ 125 mm, and the mass loading was ~ 54 mg·cm^{-2}. A thin Au film was sputtered on the surface of the NMC811/LiBO$_x$/ITO composite cathode prior to the electrochemical test. The sputtering process was performed at 20 mA for 120 s.

2.2 Characterization

The crystal structures of the synthesized LATP, poly(ethylene oxide) (PEO)/LATP, lithium boron hydroxide, ITO and their composites were characterized by X-ray diffraction (XRD) (Cu Kα, λ ~ 0.15406 nm). Raman spectra (Horiba evolution, 532 nm) were carried out to further characterize the phase of LBO$_x$. The morphologies of LCO/LBO$_x$/ITO, NMC811/LBO$_x$/ITO, and PEO/LATP were examined using field-emission scanning electron microscopy (FESEM, JSM-7600F) equipped with energy dispersive X-ray spectroscopy (EDS) capability. The microstructures and compositions of NMC811/LBO$_x$/ITO were analyzed by transmission electron microscopy (TEM) equipped with EDS (FEI Titan 300 kV). Solid-state nuclear magentic resonance (NMR) experiments were carried out to examine the reaction between LiOH and H_3BO_3. ^{1}H NMR spectra were recorded on a Bruker Avance III HD 300 MHz spectrometer equipped with a resonance probe of Larmor frequency ν_0 = 300.2 MHz for ^{1}H resonance. For the ^{1}H spectrum, recycling delays of 5 s and a preacquisition delay of 6.5 μs were employed to accumulate 128 transients. The ^{1}H chemical shift was referenced using adamantane. Time-of-flight secondary ion mass spectrometry (TOF-SIMS) was carried out to analyze the surface composition of NMC811/LBO$_x$/ITO, and a Bi^+ ion beam (30 keV ion energy, ~ 2 nA measured sample current) was used to analyze 100 μm × 100 μm areas during a 10 min acquisition time. The electronic conductivity of ITO was tested by the *I*–*V* method, estimated by the formula $\sigma = d/RA$, where d is the pellet thickness, A is the surface area, and R is the resistance obtained from the measurements. The surface energy was tested on a Drop Shape Analyzer (KRUSS DSA100) with water and diiodomethane liquids. The chemical compositions of NMC811, NMC811/LBO$_x$/ITO-350 °C and NMC811/LBO$_x$/ITO-800 °C were examined by inductively coupled plasma optical emission spectrometer (ICP-OES, Varian VISTA-MPX). To test the mechanical property of the sintered NMC811/LBO$_x$/ITO composite cathode, atomic force microscopy (AFM, Bruker Dimension Icon) was carried out.

2.3 Electrochemical test

All electrodes were assembled in CR2025 coin-type solid-state cells with Li metal as counter electrodes in an Ar-filled glovebox (H_2O, O_2 < 0.5 ppm). To synthesize a PEO/LATP composite SSE, 0.6 g PEO powder, 0.4 g lithium bis(trifluoromethane sulfonimide) (LiTFSI), and 0.2 g LATP nanoparticles were directly dissolved in acetonitrile and stirred at 60 °C for 24 h. Then, the slurry was cast on a clean Teflon film, and a PEO/LATP film with a thickness of ~ 50 μm was successfully fabricated after vacuum drying at 60 °C for 24 h. The PEO/LATP film was then cut into small disks with a diameter of 20 mm and stored in a glovebox before use. The PEO/LATP SSE was inserted between LCO/LBO$_x$/ITO or NMC811/LBO$_x$/ITO and Li metal. The cycling voltage window was 2.8–4.2 V for LCO/LBO$_x$/ITO and 2.5–4.4 V for NMC811/LBO$_x$/ITO. All solid cells were tested at a temperature of 50 °C. Electrochemical impedance spectroscopy (EIS) tests were performed using an electrochemical workstation (Biologic SP-300) between 7 MHz and 0.1 Hz with an alternating current (AC) amplitude of 20 mV. The diffusion coefficient of LBO$_x$ was calculated based on the following equations: $D_{Li^+} = \frac{R^2T^2}{2A^2n^4F^4C^2\sigma^2}$, and $Z_{re} = R_{SE} + R_{ct} + \sigma\omega^{-0.5}$, in which R, T, A, n, F, and C are the gas constant, absolute temperature, surface area of the electrodes, the number of electrons, Faraday constant, and Li-ions concentration, respectively; and σ is the Warburg factor calculated by the fitted linear relationships between real resistance (Z_{re}) and inverse square root of the angle frequency ($\omega^{-0.5}$). Galvanostatic intermittent titration technique (GITT) technique was applied to determine the Li^+ ion diffusion coefficients (D_{Li^+}) in the NCM811/LBO$_x$/ITO cathode. A current pulse (0.01 A·g^{-1}) of 0.5 h followed by 3 h of relaxation time was repeatedly applied. The D_{Li^+} could be calculated according to the following equation: $D_{Li^+} = \frac{4}{\pi\tau}\left(\frac{n_M V_M}{S}\right)^2\left(\frac{\Delta E_s}{\Delta E_\tau}\right)^2 (\tau \ll L^2/D)$, where τ equals to 600 s, n_M and V_M are the moles and molar volume of NCM811/LBO$_x$/ITO, S is the geometric area of the electrodes (1.13 cm^{-2}), ΔE_τ is total change of cell voltage during constant

current pulse neglecting the *IR*-drop), and ΔE_s is the change of the steady-state voltage. The activation energy (E_a) of PEO/LATP solid electrolyte was calculated from the Arrhenius equation: $\sigma = A\exp\left(\frac{-E_a}{k_b T}\right)$, where σ, A, k_b, T, and E_a represent the ionic conductivity, pre-exponential factor, the Boltzmann constant, the absolute temperature, and the activation energy, respectively.

2.4 Computational method

All calculations were performed with the Vienna *ab initio* simulation package (VASP) based on density functional theory (DFT) [39] within the generalized gradient approximation of the Perdew–Burke–Ernzerhof (PBE) functional [40]. The interaction between ion cores and valence electrons was treated using the projector augmented wave (PAW) method [41]. DFT+U was applied for the 3d orbitals of Ni (U = 6.0 eV and J = 0 eV) [42]. The plane-wave cutoff energy was set to be 520 eV. The structures were relaxed until all the atomic forces on each ion were less than 0.02 eV·Å^{-1}, and the energy convergence with the energy difference was below 10^{-5} eV. The (104) surface of the layered $LiNiO_2$ was simulated by a supercell that contained 24 Li, 24 Ni, and 48 O atoms, and the vacuum layer in the z-direction was approximately 20 Å to avoid the interaction between vertically periodic images. To simulate the $LiBO_2$/$LiNiO_2$ interface, a $LiBO_2$ slab containing 14 Li, 24 B, and 48 O atoms was stacked on the surface of a $LiNiO_2$ (104) slab containing 24 Li, 24 Ni, and 48 O atoms. The Brillouin zone was sampled with a 1 × 3 × 1 k-point mesh by the Monkhorst–Pack grid for geometry optimization. Throughout the simulations, van der Waals (vdW) interactions at the DFT-D2 level were taken into account [43–45]. The atomic structures were visualized and plotted using VESTA.

3 Results and discussion

3.1 The effects of the low-melting-point additives and ITO nanoparticle coating

To reveal its structural evolution of LiOH and H_3BO_3 composite additive, XRD, Raman spectra, X-ray photoelectron spectroscopy (XPS) and solid-state NMR spectroscopy were performed. Monoclinic phase lithium boron hydroxide with a composition of $LiB_5O_7(OH)_2$ formed at 200 °C, while some nonreacted LiOH was detected (Fig. 2(a)). At a temperature above 350 °C, $Li_2B_4O_7$ with a tetragonal crystalline structure was detected to be the main component with some amount of monoclinic $LiBO_2$ (Fig. 2(b)). With increased temperature, the $LiBO_2$ ratio increases. Raman spectra was carried out to further characterize the phase of LBO_x synthesized from 350 to 800 °C (Fig. 2(c)). For LBO_x sintered at 350 °C, two obvious bands at 778 and 721 cm^{-1} are due to the groups of six-membered rings with one BO^{4-} tetrahedron and metaborate chain [46, 47], respectively. The groups of six-membered rings with one BO^{4-} tetrahedron is attributed to the

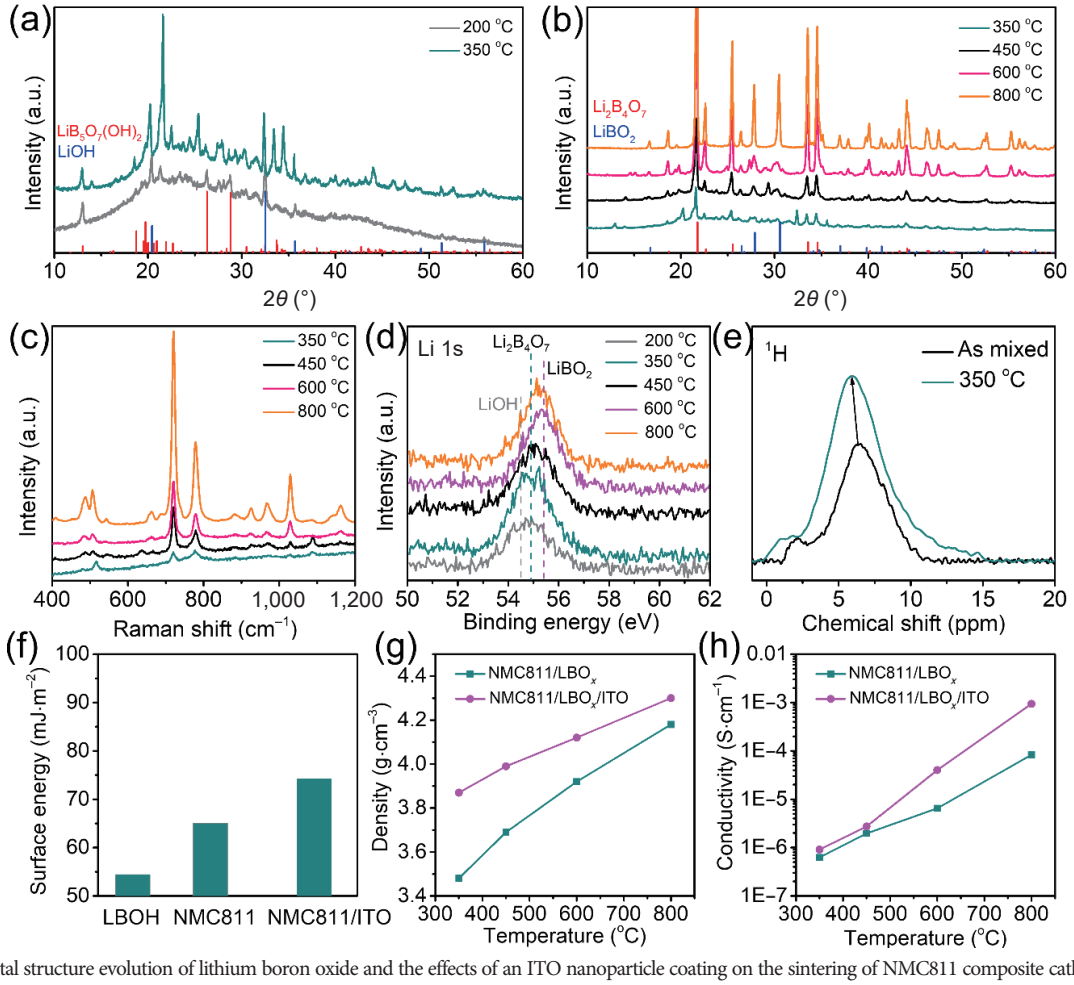

Figure 2 Crystal structure evolution of lithium boron oxide and the effects of an ITO nanoparticle coating on the sintering of NMC811 composite cathodes. (a) XRD diffraction patterns of LiOH and H_3BO_3 composite calcined at 200 and 350 °C. (b) XRD diffraction patterns of LiOH and H_3BO_3 composite calcined at 350 and 800 °C. (c) Raman spectra of the as synthesized LBO_x at varying temperatures. (d) Li 1s XPS spectra of LiOH and H_3BO_3 composite calcined calcined from 200 to 800 °C. (e) ^{1}H NMR spectrum of the as-mixed LiOH and H_3BO_3 composite and that calcined at 350 °C. (f) Surface energy comparison of the as-mixed LiOH and H_3BO_3 composite, NMC811 and NMC811/ITO composites. (g) Density of NMC811/LBO_x with and without ITO nanoparticle coating at elevated temperatures from 350 to 800 °C. (h) Conductivity of NMC811/LBO_x with and without ITO nanoparticle coating at elevated temperatures from 350 to 800 °C.

$Li_2B_4O_7$ glass with a relative low Li content. The band at 515 cm^{-1} is corresponded to the group of isolated diborate. With increased temperature from 450 to 800 °C, the band intensity between 920 and 968 cm^{-1} becomes strong, indicating the formation of orthoborate that is the main structure group of $LiBO_2$ with a high Li/B ratio [48]. The Raman spectra further confirmed that the structure of the synthesized $LiBO_x$ consists of $Li_2B_4O_7$ and $LiBO_2$.The XPS spectra further confirmed the above chemical reactions. Regarding the Li 1s spectra in Fig. 2(d), the main peaks shift to $Li_2B_4O_7$ and $LiBO_2$ at 350 and 600 °C, respectively. The LiOH signal was observed below 600 °C, and the excess LiOH continuously reacted with boron oxide and formed lithium boron oxide with a higher molar ratio of Li to B at elevated temperatures. The ^1H solid-state NMR spectrum of obviously shifted from 6.4 to 5.9 ppm (Fig. 2(e)), further demonstrating the reaction of LiOH. The composite additive shows an extremely low surface energy of 55 $mJ·m^{-2}$ (Fig. 2(f)). According to the dihedral angle equation at the liquid–solid interfaces [49], additives with a lower γ_{sl} should have wettability in contact with single-crystal NMC811 particles (shown in Fig. S1 in the Electronic Supplementary Material (ESM)) during low-temperature sintering. In addition, electrically conductive ITO nanoparticles were coated on the surface of NMC811. The XRD diffraction peaks of ITO (Fig. S2(a) in the ESM) show characteristic patterns of In_2O_3 and SnO_2. Also, in the high-resolution TEM image two different line spacings of 0.5 and 0.35 nm were observed (Fig. S2(b) in the ESM), which are corresponded to In_2O_3 (200) and SnO_2 (110). Both XRD and TEM confirm the phase nature of ITO. With the ITO particles coating, the surface energy of NMC increased from 65 to 74 $mJ·m^{-2}$ that further promoted the wetting property of the grains. It is known that surface energy is related with crystal structure, surface morphology or roughness and elemental composition. For the single crystal NMC811 with smooth surface, the coating nano-sized ITO particles not only increase surface area but also improve the surface roughness, which may increase the surface free energy. The liquid-phase sintering was enabled by the composite additives and ITO nanoparticle coating resulted in densely packed NMC811 pellets. For example, as shown in Fig. 2(g), the densities of NMC811/LBO_x/ITO are 3.87, 3.99, 4.12, and 4.3 $g·cm^{-3}$ when sintered at 350, 450, 600, and 800 °C, respectively. Without ITO coating, the NMC811/LBO_x pellets show lower densities of 3.48, 3.69, 3.92, and 4.18 $g·cm^{-3}$ when sintered at 350, 450, 600, and 800 °C, respectively.

The ITO nanoparticle coating was demonstrated to enhance the electrical conductivity of the NMC811 cathode. Both EIS (Fig. S3(a) in the ESM) and direct current (DC) polarization (Fig. S3(b) in the ESM) were used to test the intrinsic ionic conductivity of ITO, the electronic conductivity calculated from EIS and DC polarization were 10.53 and 10.58 $S·cm^{-1}$, respectively. The high intrinsic electrical conductivity of ITO can be used to bridge poorly electronically contacted regions in an NMC811 electrode; that is, the ITO nanoparticle coating with a highly crystalline nature has the function of an electronic pathway. The conductance of ITO-coated NMC811 obeys the following: $G = \left(\frac{\sigma_{NMC811}}{d_{NMC811}} + \frac{\sigma_{ITO}}{d_{ITO}}\right)$, where d is the diameter and σ is the conductivity of the NMC811 or ITO film. The diameters of the NMC811 particles and ITO were ~ 1 μm and ~ 50 nm, respectively. The electrical conductivity of NMC811 varied between 10^{-6} and 10^{-4} $S·cm^{-1}$, depending on the state of charge of the material [50, 51]. This value is more than 5 orders of magnitude lower than that of ITO. Hence, an ITO film of 1 nm provides enhanced conductance parallel to any NMC811 electrode thinner than 100 μm. Note that the coating nature of ITO here is a noncontinuous particle configuration, and the electrical conductivity improved here will be smaller than that of the ITO film coating. The impedance of NMC811/LBO_x pellets with and without ITO is shown in Fig. S4 in the ESM. As calculated in Fig. 2(f), the conductivities of NMC811/LBO_x/ITO pellets are 9.1×10^{-6}, 2.73×10^{-5}, 4.01×10^{-4}, and 9.4×10^{-3} $S·cm^{-1}$ when sintered at 350, 450, 600, and 800 °C, respectively. The conductivities of the NMC811/LBO_x pellets without ITO coating are much lower, namely, 6.25×10^{-6}, 1.96×10^{-5}, 6.5×10^{-5}, and 8.3×10^{-4} $S·cm^{-1}$ when sintered at 350, 450, 600, and 800 °C, respectively. EIS (Fig. S5 in the ESM) was carried out to determine the Li-ion diffusion coefficients of LBO_x at 350 and 800 °C. The calculated diffusion coefficient (D_{Li^+}) are 6.94×10^{-15} and 1.12×10^{-14} $cm^2·S^{-1}$ for LBO_x sintered at 350 and 800 °C, respectively. It is concluded that both densely packed NMC811/LBO_x/ITO pellets and mixed-conductive interphases were successfully fabricated, which was enabled by a liquid-phase sintering technique with low-melting-point additive and ITO coating. The highly conductive and compact NMC811/LBO_x/ITO composite cathode with mixed-conductive interphases is expected to contribute to high mass loading and specific capacity, which results in high area capacity and energy density.

3.2 Scalable manufacturing of high-voltage single-crystal Ni-rich cathode solid-state electrodes enabled by low-temperature liquid-phase sintering

Figure 3 shows the morphology of the as-fabricated NMC811/LBO_x/ITO composite cathode directly sintered on Au/carbon-coated Al foil. The Au/carbon coating film used here prevents the reaction between LiOH and Al foil, which may form a high-resistance Li–Al layered double hydroxides compound [52, 53]. With the slurry-cast single-crystal NMC811, LiOH, H_3BO_3, and ITO composites on Al, under a low temperature of 350 °C, the LiOH and H_3BO_3 composite melts and infuses into the electrode and completely wets the interfaces of NMC811 and ITO nanoparticles. After cooling, the NMC811 particles were embedded uniformly in the LBO_x matrix, and no voids or cracks were observed (Fig. 3(a)). Such perfect wetting reduces the interfacial impedance at the multiple interfaces between active materials, SSE and ITO nanoparticles. At the electrode scale, the cross-sectional SEM image and corresponding elemental mapping shown in Fig. 3(b) reveal that uniformly distributed NMC811 particles were successfully covered by ITO nanoparticles and melt-infiltrated by LBO_x. No change in the crystallinity of NMC811 took place during melt infiltration, as evidenced by the XRD patterns (Fig. S6 in the ESM). For the TEM image of a single NMC811/LBO_x/ITO particle (Fig. 3(c)), the NMC811 particle was coated by ITO nanoparticles and LBO_x. Both the NMC811 and ITO particles were fully covered by LBO_x due to the good wettability, even though ITO showed a separate configuration. At a high magnification (Fig. 3(d)), LBO_x was found to have a thickness of 7 nm and strongly bonded to NMC811 and ITO particles. For the high-resolution TEM images shown in Figs. 3(e) and 3(f), crystalline planes with d-spacings of 0.2 and 0.5 nm were observed, corresponding to NMC811 (104) and In_2O_3 (200), respectively. The high-angle annular dark-field (HAADF) TEM image and related EDS elemental mapping (Fig. 3(g)) further demonstrated good wettability of LBO_x and ITO nanoparticle coating on the surface of single-crystal NMC811. The shapes of the Ni, Co, and Mn signals were the same as those of the NMC811 core, while the In and Sn signals are not uniform revealing the nanoparticle coating morphology of ITO. The outline of the band B signal covered not only NMC811 but also ITO nanoparticles, implying the uniform and complete coating of LBO_x. We

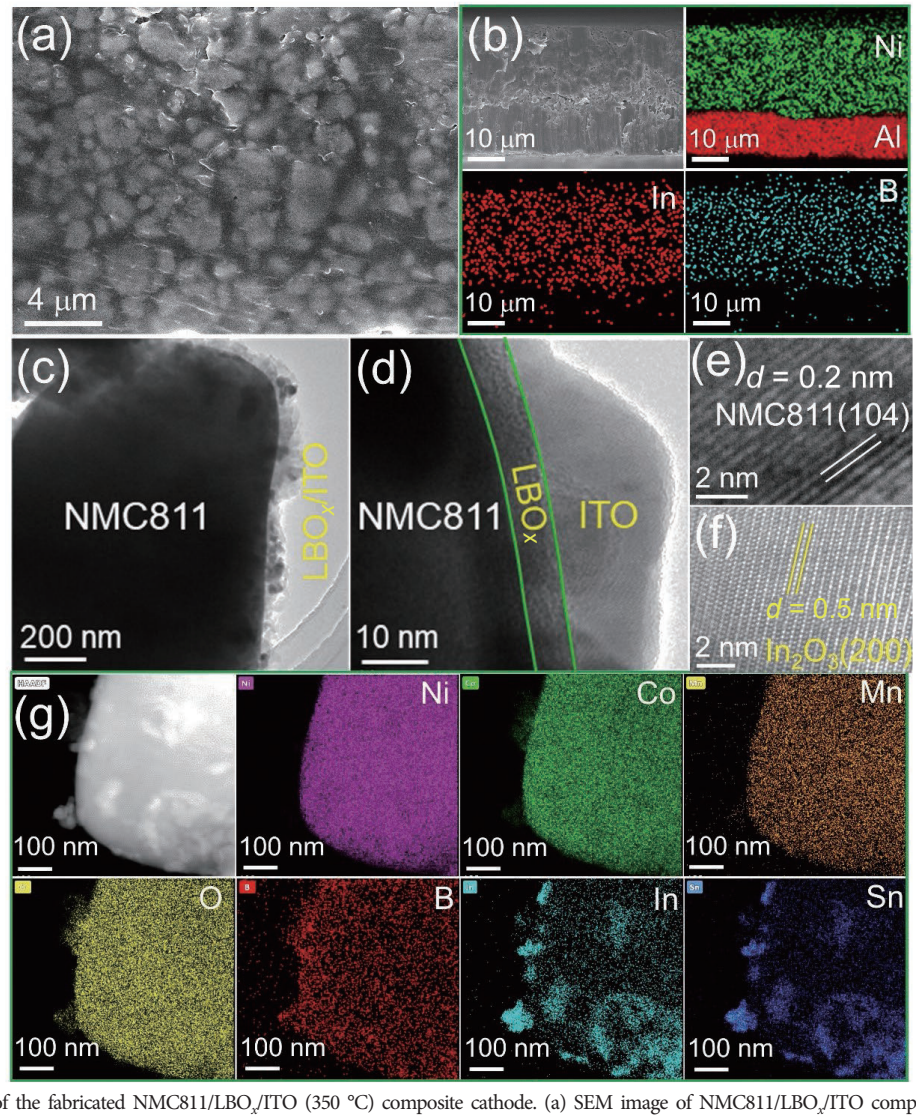

Figure 3 Morphology of the fabricated NMC811/LBO_x/ITO (350 °C) composite cathode. (a) SEM image of NMC811/LBO_x/ITO composite cathode. (b) Cross-sectional SEM image of the NMC811/LBO_x/ITO composite cathode on Al foil and corresponding elemental mapping of Ni, Al, In, and B. (c) TEM image of NMC811/LBO_x/ITO particle. (d) TEM image showing the interfaces between NMC811 and the LBO_x/ITO coating. (e) High-resolution TEM image of NMC811 in (d). (f) High-resolution TEM image of ITO in (d). (g) HAADF TEM image of NMC811/LBO_x/ITO and corresponding elemental mapping of Ni, Co, Mn, O, B, In, and Sn.

fabricated and demonstrated that LBO_x not only serves as a binder that improves the structural integrity and mechanical stability but also facilitates Li-ion transport between contacted NMC811; moreover, ITO nanoparticles can function as electronic pathways that enhance the electrical conductivity of the composite cathode. A manufacturing technique based on melt infiltration that enables both NMC811/LBO_x/ITO composite cathodes and the formation of mixed conductive interphases has thus been designed; more importantly, the method applied here is compatible with traditional slurry casting and calendaring technology.

To test the NMC811/LBO_x/ITO (350 °C) cathode in a solid cell, a PEO/LATP composite SSE with a thickness of 50 μm was fabricated (Fig. S7(a) in the ESM). The incorporation of ionically conductive and pure-phase LATP nanoparticles (Fig. S7(b) in the ESM) into the PEO matrix improved the mechanical strength and ionic conductivity. As shown in Fig. 4(a), the resistances of PEO/LATP are 63.2, 43.4, 31.0, and 22.4 Ω·cm^2 at 30, 40, 50, and 60 °C, respectively. Figure 4(b) shows the Arrhenius plot (ln(R^{-1}) vs. 1,000/T) of PEO/LATP, with an estimated activation energy of 28.75 kJ·mol^{-1}. PEO/LATP showed good cycling stability against Li metal anodes (Fig. S8 in the ESM). Not a single drop of ionic liquid or gel electrolyte was utilized in the solid-state cells, in contrast to the majority of other reported SSB studies. ICP-OES was used to examine the elemental contents, the results are shown in Table S1 in the ESM. The chemical ratio of pristine NMC is $LiNi_{0.84}Co_{0.07}Mn_{0.09}O_{2.09}$. For the NMC811/$LBO_x$/ITO-350 °C assuming the Ni ratio in the NMC is constant, the Ni content of the coated samples decreased to 46.879 wt.%, so the content of coating materials is 5.5 wt.%. The Li ratio increased to 7.385 wt.%, there may exist excess LiOH. In a recently published paper [54], the excessive LiOH was demonstrated to penetrate and coat on the surface of NMC811, resulting in preventing the solid electrolyte from oxidation. The interfacial impedance of the as-assembled solid-state NMC811/LBO_x/ITO cell is shown in Fig. 4(c). The semicircles at high frequency and low frequency are attributed to the resistance of the PEO/LATP SSE and the multiple interfaces of both the cathode/SSE and Li/SSE. The interfacial resistance here is on the same order as that of the NMC liquid cell, revealing fast electron/Li ion transport. All solid-state cells were tested at 50 °C within a wide voltage window of 2.5–4.4 V, and 1 C was defined as 200 mAh·g^{-1} in the following context. At a current rate of 0.05 C, the NMC811/LBO_x/ITO electrode showed an initial specific capacity of 207 mAh·g^{-1} with a Coulombic efficiency of 84.5% (Fig. 4(d)). After 40 cycles, the specific capacity remained at 166.9 mAh·g^{-1}. The charge–discharge curves of the NMC811/LBO_x/ITO solid-state electrode (Fig. 4(e)) exhibited a

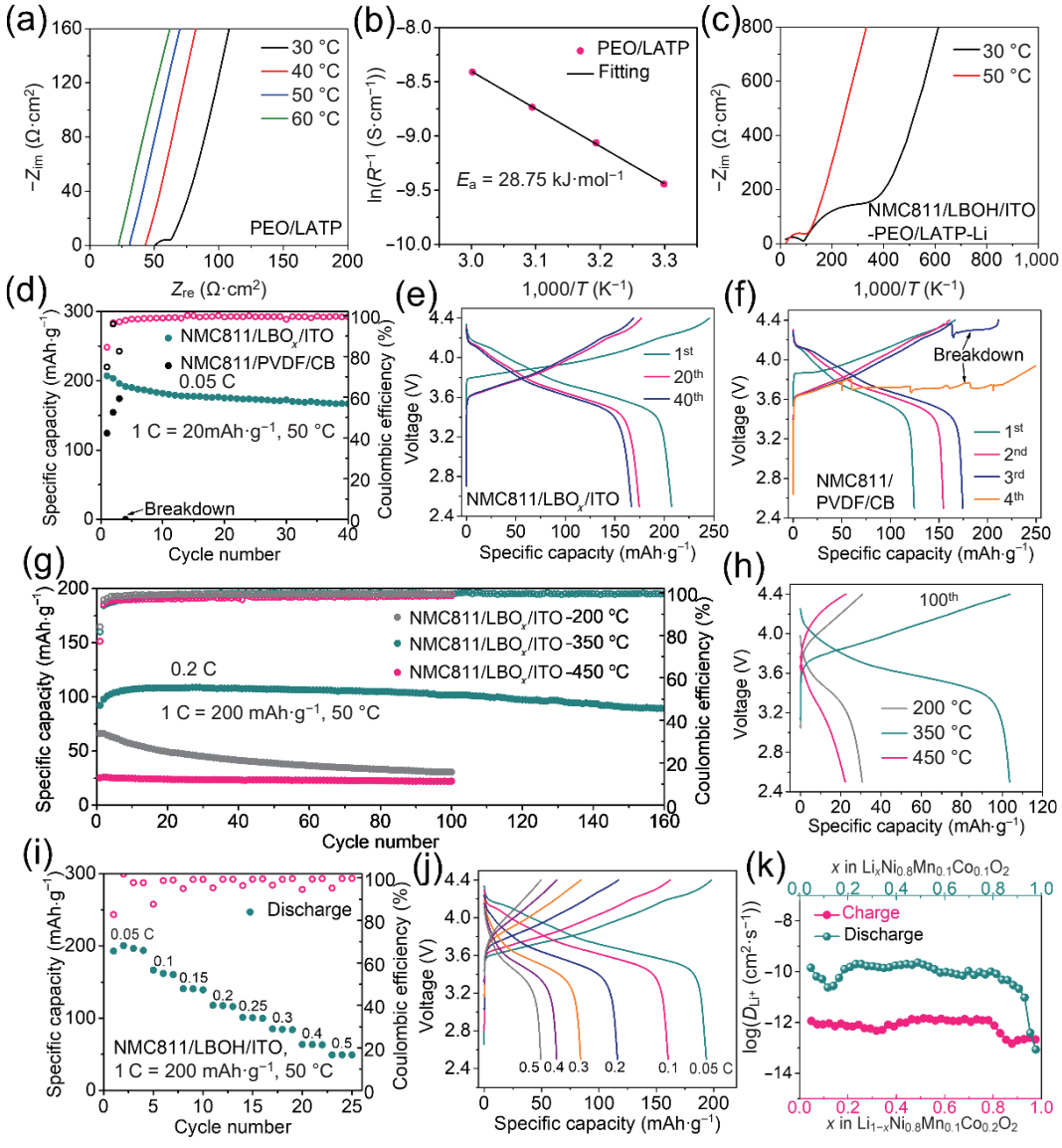

Figure 4 The solid-state electrochemical performance of the NMC811/LBO$_x$/ITO (350 °C) composite cathode. (a) Impedance test of PEO/LATP SSE at different temperatures. (b) Arrhenius plots of ionic conductivities of PEO/LATP SSE. (c) The impedance of NMC811/LBO$_x$/ITO SSB at 30 and 50 °C. (d) The cycling performance of NMC811/LBO$_x$/ITO and NMC811/PVDF/CB SSBs at 0.05 C (1 C = 200 mAh·g^{-1}) in a voltage window of 2.5–4.4 V at 50 °C. (e) Charge–discharge profiles of the NMC811/LBO$_x$/ITO SSB in (d). (f) Charge–discharge profiles of the NMC811/PVDF/CB SSB in (d). (g) Long-term cycling performance of NMC811/LBO$_x$/ITO SSBs sintered at 200, 350, and 450 °C at a rate of 0.2 C. (h) Charge–discharge profiles of NMC811/LBO$_x$/ITO sintered at 200, 350, and 450 °C SSBs in (g). (i) The rate performance of NMC811/LBO$_x$/ITO SSB. (j) Charge–discharge profiles of NMC811/LBO$_x$/ITO SSB at different current rates. (k) Calculated diffusion coefficient from GITT of NMC811/LBO$_x$/ITO.

typical shape compared with that of other reported single-crystal NMC811 cathodes in liquid cells, and the average discharge voltages at the 1st, 20th, and 40th cycles were 3.72, 3.70 and 3.67 V, respectively. In a sharp contrast, the NMC811/PVDF/CB cathode only delivered a specific capacity of 124 mAh·g^{-1} because its interfacial impedance was nearly an order higher than that of NMC811/LBO$_x$/ITO (shown in Fig. S9 in the ESM). Obvious decomposition of PEO was observed during the second charge process (Fig. 4(f)) due to the lack of LBO$_x$ and LiOH protection. At the 4th cycle, the NMC811/PVDF/CB electrode completely broke down due to the continuous decomposition of PEO.

The long-term cycling performance of NMC811/LBO$_x$/ITO is shown in Fig. 4(g). A specific capacity of 99 mAh·g^{-1} was retained after 160 cycles, which represents no capacity fade compared to the initial cycle at 0.2 C. Sintering of NMC811 composite cathode at 200 °C led to a low specific capacity and quick capacity fading during the first 20 cycles was observed and only 30.6 mAh·g^{-1} maintained after 100 cycles at 0.2 C (Fig. 4(h)). This may be caused by the lack of continuous mixed-conductive LBO$_x$/ITO interphases. However, the NMC811/LBO$_x$/ITO electrode sintered at 450 °C showed a very low capacity of 22.3 mAh·g^{-1} after 100 cycles (Fig. 4(h)). The carbon/Au coating film used here prevents the reaction between LiOH and Al foil and shows resistance to the formation of high-resistance Li–Al layered double hydroxides compounds [52, 53]. As shown in Fig. S10 in the ESM, NMC811/LBO$_x$/ITO directly sintered on pure Al foil only delivered an initial specific capacity and Coulombic efficiency of 79 mAh·g^{-1} and 57.2%, respectively, due to a large polarization.

The mixed ionic-electronic conductive interphases of NMC811/LBO$_x$/ITO (350 °C) enabled favorable rate performance in a solid-state cell. As shown in Fig. 4(i), the specific capacities of NMC811/LBO$_x$/ITO are 193.7, 160.4, 116.2, 84, 63.1, and 49.1 mAh·g^{-1} at 0.1, 0.2, 0.3, 0.4 and 0.5 C, respectively. The corresponding charge–discharge voltage profiles at 0.1, 0.2, 0.3, 0.4, and 0.5 C are shown in Fig. 4(j), with average discharge voltages of 3.72, 3.60, 3.53, 3.49 and 3.43 V, respectively. To understand the rate performance of NMC811/LBO$_x$/ITO, the GITT was carried out to determine the diffusion coefficient with

different Li contents (Fig. S11 in the ESM). As shown in Fig. 4(k), during the discharge process, the diffusion coefficient was typically 10^{-10} $cm^2 \cdot S^{-1}$ before a drop off for $x > 0.8$, causing slow Li kinetics, thereby leading to the first capacity loss [55]. The trend of the Li coefficient variation at different Li contents was similar to that in liquid cells, implying that solid-state lithiation does not change the lithiation mechanism.

This liquid-phase sintering technology can also be applied to a single-crystal LCO cathode; the SEM image of pristine LCO particles is shown in Fig. S12 in the ESM. After melt infusion of LBO_x into ITO-coated LCO, the LCO embedded uniformly in the LBO_x framework should enable fast Li ion/electron transport at the SSE/LCO interfaces (Fig. S13 in the ESM). When tested in a solid-state cell, the interfacial resistance was 530 and 231 $\Omega \cdot cm^{-2}$ at 30 and 50 °C (Fig. S14 in the ESM), respectively. At a rate of 0.05 C (1 C = 140 $mAh \cdot g^{-1}$), the initial capacity was 124 $mAh \cdot g^{-1}$, with a Coulombic efficiency of 87.4% (Fig. S15 in the ESM). When the current was increased to 0.1 C, the specific capacity was 105 $mAh \cdot g^{-1}$ and was maintained at 79 $mAh \cdot g^{-1}$ after 120 cycles.

3.3 Free-standing and dense NMC811 composite cathode enabled by high-temperature liquid-phase sintering

To design SSBs that have extremely high energy density, free-standing thick and densely packed solid-state composites are a key enabling technology, with which we can use very thin (< 10 μm) SSE films. Surprisingly, liquid-phase sintering technology with the LiOH and H_3BO_3 additive and ITO coating on NMC811 enabled us to prepare millimeter-thick NMC811/LBO_x/ITO cathodes in a free-standing configuration (see the inset in Fig. 5(a)) at a temperature of 800 °C. Taking advantage of the dense packing and high mechanical strength, the NMC811/LBO_x/ITO cathode maintained its free-standing state after polishing to ~ 125 μm thick. This result indicates that we can achieve safe and high-energy-density SSBs. The NMC811/LBO_x/ITO pellet showed a densely packed configuration, and the primary single-crystal NMC811 grains grew together and were strongly interconnected by the *in situ*-formed LBO_x phases. The mixed conductive interphases and compact nature facilitate fast Li^+/electron transport; thus, a total conductivity of 0.94×10^{-3} $S \cdot cm^{-1}$ was delivered. TOF-SIMS was employed to study the surface composition of NMC811/LBO_x/ITO (Fig. 5(c)). The Li distribution revealed the uniform distribution of single-crystal NMC811 particles and the $LiBO_x$ interphase. The signal of B covered both the Ni and In signal shapes, implying the complete coating nature of LBO_x. The EDS elemental mapping in Fig. S16 in the ESM further confirms that the NMC811 particles were fully covered by ITO and strongly bonded with LBO_x, ultimately resulting in a compact, free-standing cathode. No change in the NMC811 crystalline structure was observed after liquid-phase sintering, as confirmed by the XRD patterns in Fig. S17 in the ESM. To test the mechanical property of the sintered NMC811/LBO_x/ITO composite cathode, AFM was carried out. For the composite cathode sintered at 350 °C shows a relatively dispersive morphology (Fig. 5(d)), the corresponding Derjaguin–Müller–Toporov (DMT) modulus is 3,759 MPa (Fig. 5(e)). By contrast, the composite cathode sintered at a higher temperature at 800 °C shows a dense morphology with smooth crystals observed (Fig. 5(f)), indicating the strong bonding nature between different crystals. As a result, the composite cathode sintered at 800 °C exhibits a higher DMT modulus of 4,674 MPa (Fig. 5(g)). High temperature sintering not only improves the

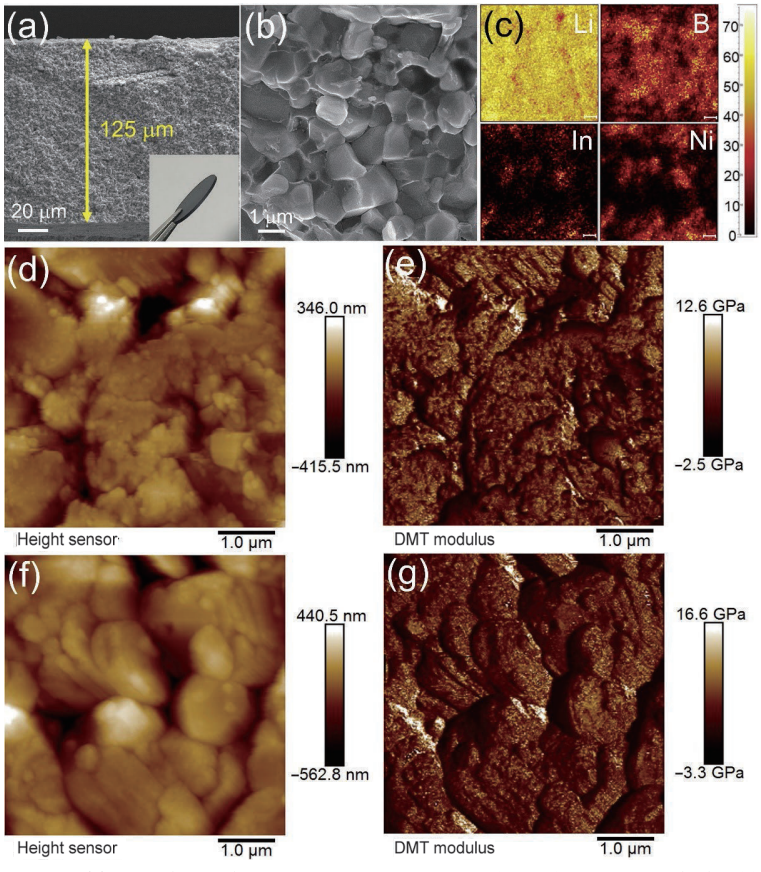

Figure 5 Fabrication and characterization of free-standing and compact NMC811/$LiBO_x$/ITO (800 °C) composite cathodes. (a) Cross-sectional SEM image of the NMC811/$LiBO_x$/ITO composite cathode; the inset is a photograph of the sintered pellet. (b) High-resolution SEM image of the NMC811/$LiBO_x$/ITO composite cathode. (c) TOF-SIMS elemental mapping of NMC811/$LiBO_x$/ITO pellets: Li, B, Ni, and In. The scale bar is 10 μm. (d) AFM image of NMC811/LBO_x/ITO pellet sintered at 350 °C. (e) The DMT modulus mapping of the area in (d). (f) AFM image of NMC811/LBO_x/ITO pellet sintered at 800 °C. (g) The DMT modulus mapping of the area in (f).

conductivity but also enhances the mechanical strength of NMC811/LBO_x/ITO composite cathode.

The solid-state electrochemical performance of the NMC811/$LiBO_x$/ITO (800 °C) cathode was also tested using a PEO/LATP SSE paired with a Li metal anode. ICP-OES was used to examine the elemental contents, the results are shown in Table S1 in the ESM. For the NMC811/LBO_x/ITO–800 °C, assuming the Ni ratio in the NMC is constant, the Ni content of the coated samples decreased to 46.487 wt.%, so the content of coating materials is 6.3 wt.%. The Li ratio increased to 7.138 wt.% for NMC811/LBO_x/ITO-800 °C. At 800 °C, the LiOH precursor mainly compensated the Li loss during high temperature sintering and react with boron oxide. The mass loading in this case was 54 mg·cm^{-1} based on the total mass of NMC811, $LiBO_x$ and ITO. At a low current of 0.02 C (Fig. 6(a)), an initial specific capacity of 174 mAh·g^{-1} with a Coulombic efficiency of 75% was observed. When the current was increased to 0.05 C, the specific capacity was 120.9 mAh·g^{-1}, and no capacity fading was observed after 30 cycles. During a long-term cycling, the thick and densely packed NMC811/LBO_x/ITO electrode, the cell delivered a capacity of 61 mAh·g^{-1} after 60 cycles at 0.1 C (Fig. S18 in the ESM). The polarization voltage was larger than that of the NMC811/LBO_x/ITO cathode on the Al film (Fig. 6(b)). As shown in Fig. 6(c), the area capacity and voltage of NMC811/$LiBO_x$/ITO are among the best of the recent published work [13, 19, 21, 54, 56–59], revealing its great potential to achieve high energy density. Within the thick and compact NMC811/$LiBO_x$/ITO cathode, a 2 × 10 layered pouch cell was designed, and the details are described in Fig. 6(d) and Table S2 in the ESM. The pouch cell with a thick, Ni-rich NMC811/$LiBO_x$/ITO cathode, such as with a thickness exceeding 80 μm, as illustrated in Fig. 6(e), is expected to deliver a high energy density of 500 Wh·kg^{-1}.

3.4 Suppressing oxygen activity and side reactions

At the interface between the $LiNiO_2$ (104) surface and $LiBO_2$, the B atom preferentially bonds with the surface O of $LiNiO_2$ but not with Li or Ni, as shown in Fig. 7(a). The interfacial B–O bonds are stronger than the Ni–O bond, as indicated by the stronger localized electron density for the former in the electron localization function (ELF) plot (Fig. 7(b)). ELF values of 1 and 0 indicate perfectly localized and completely delocalized electrons within the bond, respectively [60]. The average B–O bond has a short bond distance (1.387 Å), and the localized electron density of O polarizes toward B, which suggests a covalent bonding nature. For the oxygen local structure, we consider two types of O coordination: Type-I lattice O is coordinated by three Ni atoms and three Li atoms (inset of Fig. 7(c)); type-II surface O (now becoming an interfacial O) is coordinated by one B atom, two Ni atoms and two Li atoms (inset of Fig. 7(d); the strong B–O bond pulls the O atom away from the center of the original "octahedral" site). Figure 7(d) shows that the strong B–O bond effectively lowers the energy of the O 2p states, which have fewer high-energy states close to E_f than that of lattice O (Fig. 7(c)). A significant energy-level lowering is achieved through the strong covalent B–O bond, which greatly stabilizes the interface O atom. The above results clearly demonstrate that the chemical nature of reactive wetting is the selective B–O bonds formed at the $LiBO_2$/$LiNiO_2$ interface, and the superior stability has an electronic structure origin that effectively suppresses interface oxygen activity. This explanation rationalizes the design of reactive-wetting lithium boron oxide coating materials with selective bonding, which not only ensures uniform complete coverage but also stabilizes the surface oxygen atoms [61]. The interfacial B–O bond was also demonstrated to suppress side reactions between NMC811 and PEO/LATP SSE, thus enabling stable cycling at a high cutoff voltage of 4.4 V.

4 Conclusions

In summary, a compatible SSB manufacturing technique including composite cathode architecture and mixed ionic-electronic interphases design enabled by liquid-phase sintering has been proposed. Low-melting-point LiOH and H_3BO_3 composite additive is utilized to infiltrate into a dense, thermally stable electrode at a moderately elevated temperature (~ 350 °C) in a liquid state, which then solidifies during cooling. In addition, the ITO nanoparticle coating not only helps to build an electronic pathway but also increases the surface energy of NMC811 powders, which further promotes the densification process. The liquid-phase sintering and ITO nanoparticle coating enable the

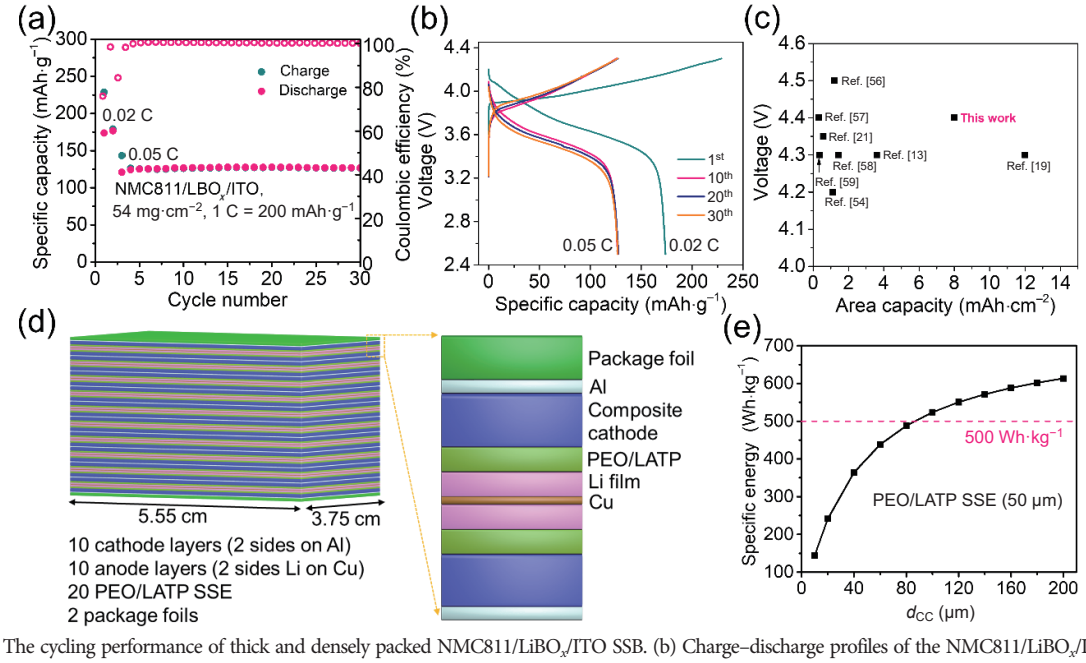

Figure 6 (a) The cycling performance of thick and densely packed NMC811/$LiBO_x$/ITO SSB. (b) Charge–discharge profiles of the NMC811/$LiBO_x$/ITO SSB in (a). (c) The voltage and area capacity comparison of this work with previous reported works. (d) Design of a pouch-type SSB with an NMC811/$LiBO_x$/ITO composite cathode, PEO/LATP SSE and thin Li film. (e) The specific energy of the pouch cell versus the composite cathode thickness with a 50 μm thick PEO/LATP SSE.

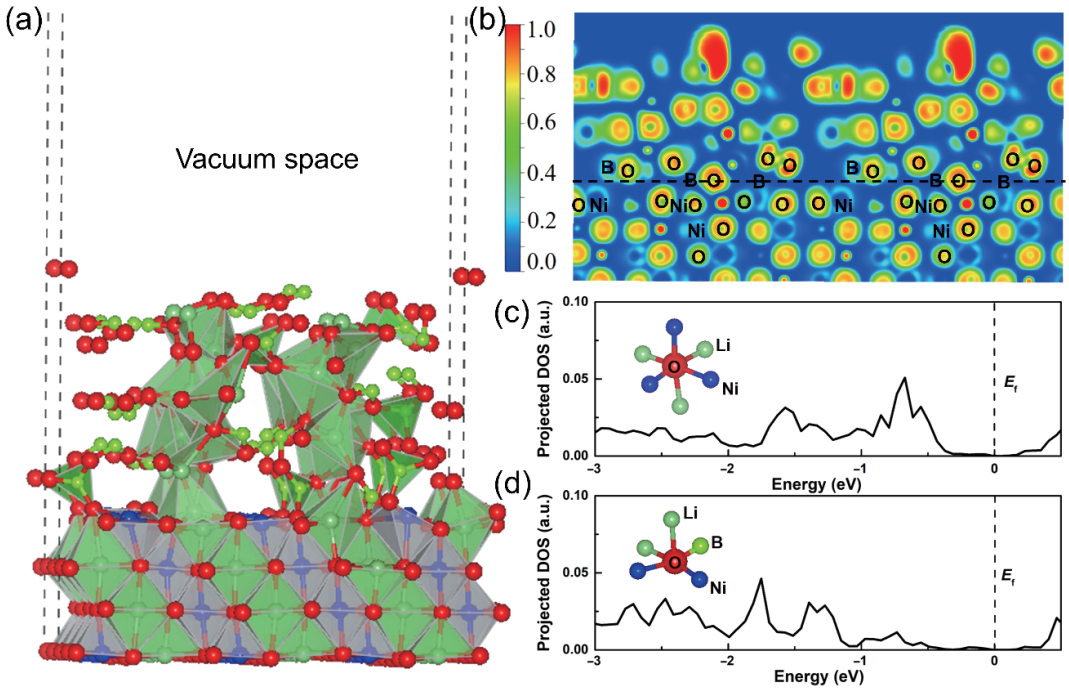

Figure 7 Interfacial B–O bond suppressing oxygen reduction. (a) Atomic structure of a simulated interface between the $LiNiO_2$ (104) surface and $LiBO_2$. (b) 2D slices of the ELF of the simulated interface in (a). (c) Projected density of states (DOS) and schematic local environment of lattice oxygen coordinated by three Ni and three Li atoms. (d) DOS and schematic local environment of interface oxygen coordinated by one B atom, two Ni atoms and two Li atoms.

fabrication of free-standing, high-density, and thick composite cathodes containing NMC811 and $LiCoO_2$ layered oxides. Tested in a solid-state cell, a high area capacity of 8 mAh·cm^{-2} within a wide voltage window up to 4.4 V is achieved, which is expected to be used to fabricate 500 Wh·kg^{-1} SSBs. The higher energy density is enabled by a new solid cell architecture design, thick and highly dense packed cathode, high specific capacity Ni-rich NMC811 active material and mixed ionic-electronic conductive interphases that not only improve the mechanical stability but also facilitate fast Li ion/electron transport. We expect that not only conventional oxide active materials but also conversion-type (e.g., S and Li_2S) cathodes will be compatible with the proposed technique here.

Acknowledgements

This research was supported by Natural Science Foundation of Jiangsu Province (No. BK20200800), the National Natural Science Foundation of China (Nos. 51902165, 12004145, 52072323, and 52122211), Natural Science Foundation of Jiangxi Province (Nos. 20192ACBL2004 and 20212BAB214032), and Nanjing Science & Technology Innovation Project for Personnel Studying Abroad. Part of the calculations were supported by the Center for Computational Science and Engineering at Southern University of Science and Technology, and high-performance computing platform of Jinggangshan University.

Electronic Supplementary Material: Supplementary material (further details of SEM imaging, EDS mapping, XRD, impedance, GITT, electrochemical test, and 2 tables) is available in the online version of this article at https://doi.org/10.1007/s12274-022-4242-5.

References

[1] Fan, L. Z.; He, H. C.; Nan, C. W. Tailoring inorganic-polymer composites for the mass production of solid-state batteries. *Nat. Rev. Mater.* **2021**, *6*, 1003–1019.

[2] Tan, D. H. S.; Banerjee, A.; Chen, Z.; Meng, Y. S. From nanoscale interface characterization to sustainable energy storage using all-solid-state batteries. *Nat. Nanotechnol.* **2020**, *15*, 170–180.

[3] Kato, Y.; Hori, S.; Saito, T.; Suzuki, K.; Hirayama, M.; Mitsui, A.; Yonemura, M.; Iba, H.; Kanno, R. High-power all-solid-state batteries using sulfide superionic conductors. *Nat. Energy* **2016**, *1*, 16030.

[4] Zhang, Q. B.; Gong, Z. L.; Yang, Y. Advance in interface and characterizations of sulfide solid electrolyte materials. *Acta Phys. Sin.* **2020**, *69*, 228803.

[5] Huang, Q.; Turcheniuk, K.; Ren, X. L.; Magasinski, A.; Song, A. Y.; Xiao, Y. R.; Kim, D.; Yushin, G. Cycle stability of conversion-type iron fluoride lithium battery cathode at elevated temperatures in polymer electrolyte composites. *Nat. Mater.* **2019**, *18*, 1343–1349.

[6] Wu, J. H.; Liu, S. F.; Han, F. D.; Yao, X. Y.; Wang, C. S. Lithium/sulfide all-solid-state batteries using sulfide electrolytes. *Adv. Mater.* **2021**, *33*, 2000751.

[7] Liu, J.; Bao, Z. N.; Cui, Y.; Dufek, E. J.; Goodenough, J. B.; Khalifah, P.; Li, Q. Y.; Liaw, B. Y.; Liu, P.; Manthiram, A. et al. Pathways for practical high-energy long-cycling lithium metal batteries. *Nat. Energy* **2019**, *4*, 180–186.

[8] Wan, H. L.; Liu, S. F.; Deng, T.; Xu, J. J.; Zhang, J. X.; He, X. Z.; Ji, X.; Yao, X. Y.; Wang, C. S. Bifunctional interphase-enabled $Li_{10}GeP_2S_{12}$ electrolytes for lithium-sulfur battery. *ACS Energy Lett.* **2021**, *6*, 862–868.

[9] Feng, X. Y.; Wu, H. H.; Gao, B.; Świętosławski, M.; He, X.; Zhang, Q. B. Lithiophilic N-doped carbon bowls induced Li deposition in layered graphene film for advanced lithium metal batteries. *Nano Res.* **2022**, *15*, 352–360.

[10] Wu, K.; Li, Q.; Dang, R. B.; Deng, X.; Chen, M. M.; Lee, Y. L.; Xiao, X. L.; Hu, Z. B. A novel synthesis strategy to improve cycle stability of $LiNi_{0.8}Mn_{0.1}Co_{0.1}O_2$ at high cut-off voltages through core–shell structuring. *Nano Res.* **2019**, *12*, 2460–2467.

[11] Shao, Y. J.; Wang, H. C.; Gong, Z. L.; Wang, D. W.; Zheng, B. Z.; Zhu, J. P.; Lu, Y. X.; Hu, Y. S.; Guo, X. X.; Li, H. et al. Drawing a soft interface: An effective interfacial modification strategy for garnet-type solid-state Li batteries. *ACS Energy Lett.* **2018**, *3*, 1212–1218.

[12] Balaish, M.; Gonzalez-Rosillo, J. C.; Kim, K. J.; Zhu, Y. T.; Hood, Z. D.; Rupp, J. L. M. Processing thin but robust electrolytes for solid-state batteries. *Nat. Energy* **2021**, *6*, 227–239.

[13] He, F.; Tang, W. J.; Zhang, X. Y.; Deng, L. J.; Luo, J. Y. High energy density solid state lithium metal batteries enabled by sub-5

μm solid polymer electrolytes. *Adv. Mater.* **2021**, *33*, 2105329.
[14] Kim, J. M.; Zhang, X. H.; Zhang, J. G.; Manthiram, A.; Meng, Y. S.; Xu, W. A review on the stability and surface modification of layered transition-metal oxide cathodes. *Mater. Today* **2021**, *46*, 155–182.
[15] Kim, U. H.; Park, G. T.; Son, B. K.; Nam, G. W.; Liu, J.; Kuo, L. Y.; Kaghazchi, P.; Yoon, C. S.; Sun, Y. K. Heuristic solution for achieving long-term cycle stability for Ni-rich layered cathodes at full depth of discharge. *Nat. Energy* **2020**, *5*, 860–869.
[16] Zhang, F.; Lou, S. F.; Li, S.; Yu, Z. J.; Liu, Q. S.; Dai, A.; Cao, C. T.; Toney, M. F.; Ge, M. Y.; Xiao, X. H. et al. Surface regulation enables high stability of single-crystal lithium-ion cathodes at high voltage. *Nat. Commun.* **2020**, *11*, 3050.
[17] Guo, F. Y.; Xie, Y. F.; Zhang, Y. X. Low-temperature strategy to synthesize single-crystal $LiNi_{0.8}Co_{0.1}Mn_{0.1}O_2$ with enhanced cycling performances as cathode material for lithium-ion batteries. *Nano Res.* **2020**, *15*, 2052–2059.
[18] Bi, Y. J.; Tao, J. H.; Wu, Y. Q.; Li, L. Z.; Xu, Y. B.; Hu, E. Y.; Wu, B. B.; Hu, J. T.; Wang, C. M.; Zhang, J. G. et al. Reversible planar gliding and microcracking in a single-crystalline Ni-rich cathode. *Science* **2020**, *370*, 1313–1317.
[19] Tan, D. H. S.; Chen, Y. T.; Yang, H. D.; Bao, W.; Sreenarayanan, B.; Doux, J. M.; Li, W. K.; Lu, B. Y.; Ham, S. Y.; Sayahpour, B. et al. Carbon-free high-loading silicon anodes enabled by sulfide solid electrolytes. *Science* **2021**, *373*, 1494–1499.
[20] Yi, M. Y.; Li, J.; Fan, X. M.; Bai, M. H.; Zhang, Z.; Hong, B.; Zhang, Z. A.; Hu, G. R.; Jiang, H.; Lai, Y. Q. Single crystal Ni-rich layered cathodes enabling superior performance in all-solid-state batteries with PEO-based solid electrolytes. *J. Mater. Chem. A* **2021**, *9*, 16787–16797.
[21] Sun, H.; Xie, X. X.; Huang, Q.; Wang, Z. X.; Chen, K. J.; Li, X. L.; Gao, J.; Li, Y. T.; Li, H.; Qiu, J. S. et al. Fluorinated poly-oxalate electrolytes stabilizing both anode and cathode interfaces for all-solid-state Li/NMC811 batteries. *Angew. Chem., Int. Edit.* **2021**, *60*, 18335–18343.
[22] Liu, X. S.; Zheng, B. Z.; Zhao, J.; Zhao, W. M.; Liang, Z. T.; Su, Y.; Xie, C. P.; Zhou, K.; Xiang, Y. X.; Zhu, J. P. et al. Electrochemo-mechanical effects on structural integrity of Ni-rich cathodes with different microstructures in all solid-state batteries. *Adv. Energy Mater.* **2021**, *11*, 2003583.
[23] Randau, S.; Weber, D. A.; Kötz, O.; Koerver, R.; Braun, P.; Weber, A.; Ivers-Tiffée, E.; Adermann, T.; Kulisch, J.; Zeier, W. G. et al. Benchmarking the performance of all-solid-state lithium batteries. *Nat. Energy* **2020**, *5*, 259–270.
[24] Han, X. G.; Gong, Y. H.; Fu, K.; He, X. F.; Hitz, G. T.; Dai, J. Q.; Pearse, A.; Liu, B. Y.; Wang, H.; Rubloff, G. et al. Negating interfacial impedance in garnet-based solid-state Li metal batteries. *Nat. Mater.* **2017**, *16*, 572–579.
[25] Li, Y. T.; Chen, X.; Dolocan, A.; Cui, Z. M.; Xin, S.; Xue, L. G.; Xu, H. H.; Park, K.; Goodenough, J. B. Garnet electrolyte with an ultralow interfacial resistance for Li-metal batteries. *J. Am. Chem. Soc.* **2018**, *140*, 6448–6455.
[26] Pan, K. C.; Zhang, L.; Qian, W. W.; Wu, X. K.; Dong, K.; Zhang, H. T.; Zhang, S. J. A flexible ceramic/polymer hybrid solid electrolyte for solid-state lithium metal batteries. *Adv. Mater.* **2020**, *32*, 2000399.
[27] Hu, C. J.; Shen, Y. B.; Shen, M.; Liu, X.; Chen, H. W.; Liu, C. H.; Kang, T.; Jin, F.; Li, L.; Li, J. et al. Superionic conductors via bulk interfacial conduction. *J. Am. Chem. Soc.* **2020**, *142*, 18035–18041.
[28] Liu, G. Z.; Shi, J. M.; Zhu, M. T.; Weng, W.; Shen, L.; Yang, J.; Yao, X. Y. Ultra-thin free-standing sulfide solid electrolyte film for cell-level high energy density all-solid-state lithium batteries. *Energy Storage Mater.* **2021**, *38*, 249–254.
[29] Wan, H. L.; Cai, L. T.; Han, F. D.; Mwizerwa, J. P.; Wang, C. S.; Yao, X. Y. Construction of 3D electronic/ionic conduction networks for all-solid-state lithium batteries. *Small* **2019**, *15*, 1905849.
[30] Zhang, C. Y.; Liu, S.; Li, G. J.; Zhang, C. J.; Liu, X. J.; Luo, J. Y. Incorporating ionic paths into 3D conducting scaffolds for high volumetric and areal capacity, high rate lithium-metal anodes. *Adv. Mater.* **2018**, *30*, 1801328.
[31] Yan, Y. Y.; Ju, J. W.; Dong, S. M.; Wang, Y. T.; Huang, L.; Cui, L. F.; Jiang, F.; Wang, Q. L.; Zhang, Y. F.; Cui, G. L. *In situ* polymerization permeated three-dimensional Li^+-percolated porous oxide ceramic framework boosting all solid-state lithium metal battery. *Adv. Sci.* **2021**, *8*, 2003887.
[32] Han, X.; Wang, S. Y.; Xu, Y. B.; Zhong, G. M.; Zhou, Y.; Liu, B.; Jiang, X. Y.; Wang, X.; Li, Y.; Zhang, Z. Q. et al. All solid thick oxide cathodes based on low temperature sintering for high energy solid batteries. *Energy Environ. Sci.* **2021**, *14*, 5044–5056.
[33] Liu, T.; Zhang, Y. B.; Zhang, X.; Wang, L.; Zhao, S. X.; Lin, Y. H.; Shen, Y.; Luo, J.; Li, L. L.; Nan, C. W. Enhanced electrochemical performance of bulk type oxide ceramic lithium batteries enabled by interface modification. *J. Mater. Chem. A* **2018**, *6*, 4649–4657.
[34] Han, F. D.; Yue, J.; Chen, C.; Zhao, N.; Fan, X. L.; Ma, Z. H.; Gao, T.; Wang, F.; Guo, X. X.; Wang, C. S. Interphase engineering enabled all-ceramic lithium battery. *Joule* **2018**, *2*, 497–508.
[35] Zhang, Q.; Cao, D. X.; Ma, Y.; Natan, A.; Aurora, P.; Zhu, H. L. Sulfide-based solid-state electrolytes: Synthesis, stability, and potential for all-solid-state batteries. *Adv. Mater.* **2019**, *31*, 1901131.
[36] Gellert, M.; Dashjav, E.; Grüner, D.; Ma, Q. L.; Tietz, F. Compatibility study of oxide and olivine cathode materials with lithium aluminum titanium phosphate. *Ionics* **2018**, *24*, 1001–1006.
[37] Feng, W. L.; Lai, Z. Z.; Dong, X. L.; Li, P. L.; Wang, Y. G.; Xia, Y. Y. Garnet-based all-ceramic lithium battery enabled by $Li_{2.985}B_{0.005}OCl$ solder. *iScience* **2020**, *23*, 101071.
[38] Xiao, Y. R.; Turcheniuk, K.; Narla, A.; Song, A. Y.; Ren, X. L.; Magasinski, A.; Jain, A.; Huang, S.; Lee, H.; Yushin, G. Electrolyte melt infiltration for scalable manufacturing of inorganic all-solid-state lithium-ion batteries. *Nat. Mater.* **2021**, *20*, 984–990.
[39] Kresse, G.; Furthmüller, J. Efficient iterative schemes for *ab initio* total-energy calculations using a plane-wave basis set. *Phys. Rev. B* **1996**, *54*, 11169–11186.
[40] Perdew, J. P.; Burke, K.; Ernzerhof, M. Generalized gradient approximation made simple. *Phys. Rev. Lett.* **1996**, *77*, 3865–3868.
[41] Blöchl, P. E. Projector augmented-wave method. *Phys. Rev. B* **1994**, *50*, 17953–17979.
[42] Liu, B.; Xu, B.; Wu, M.; Ouyang, C. Y. First-principles GGA+U study on structural and electronic properties in $LiMn_{0.5}Ni_{0.5}O_2$, $LiMn_{0.5}Co_{0.5}O_2$ and $LiCo_{0.5}Ni_{0.5}O_2$. *Int. J. Electrochem. Sci.* **2016**, *11*, 432–445.
[43] Grimme, S. Accurate description of van der Waals complexes by density functional theory including empirical corrections. *J. Comput. Chem* **2004**, *25*, 1463–1473.
[44] Shi, S. Q.; Gao, J.; Liu, Y.; Zhao, Y.; Wu, Q.; Ju, W. W.; Ouyang, C. Y.; Xiao, R. J. Multi-scale computation methods: Their applications in lithium-ion battery research and development. *Chin. Phys. B* **2015**, *25*, 018212.
[45] He, B.; Chi, S. T.; Ye, A. J.; Mi, P. H.; Zhang, L. W.; Pu, B. W.; Zou, Z. Y.; Ran, Y. B.; Zhao, Q.; Wang, D. et al. High-throughput screening platform for solid electrolytes combining hierarchical ion-transport prediction algorithms. *Sci. Data* **2020**, *7*, 151.
[46] Elalaoui, A. E.; Maillard, A.; Fontana, M. D. Raman scattering and non-linear optical properties in $Li_2B_4O_7$. *J. Phys.: Condens. Matter* **2015**, *17*, 7441.
[47] Osipov, A. A.; Osipova, L. M. Structure of lithium borate glasses and melts: Investigation by high temperature Raman spectroscopy. *Phys. Chem. Glasses: Eur. J. Glass Sci. Technol., Part B* **2009**, *50*, 343–354.
[48] Tatsumisago, M.; Takahashi, M.; Minami, T.; Tanaka, M.; Umesaki, N.; Iamoto, N. Structural investigation of rapidly quenched Li_2O-B_2O_3 glasses by Raman spectroscopy. *Yogyo Kyokaishi* **1986**, *94*, 464–469.
[49] Rahaman, M. N. *Ceramic Processing*, 2nd ed.; CRC Press: Boca Raton, 2017.
[50] Park, M.; Zhang, X. C.; Chung, M.; Less, G. B.; Sastry, A. M. A review of conduction phenomena in Li-ion batteries. *J. Power Sources* **2010**, *195*, 7904–7929.
[51] Marzec, J.; Świerczek, K.; Przewoźnik, J.; Molenda, J.; Simon, D.; Kelder, E.; Schoonman, J. Conduction mechanism in operating a $LiMn_2O_4$ cathode. *Solid State Ionics* **2002**, *146*, 225–237.
[52] Wang, S. L.; Lin, C. H.; Yan, Y. Y.; Wang, M. K. Synthesis of Li/Al LDH using aluminum and LiOH. *Appl. Clay Sci.* **2013**, *72*, 191–195.

[53] Qu, J.; He, X. M.; Wang, B. T.; Zhong, L. H.; Wan, L.; Li, X. W.; Song, S. X.; Zhang, Q. W. Synthesis of Li-Al layered double hydroxides via a mechanochemical route. *Appl. Clay Sci.* **2016**, *120*, 24–27.

[54] Zhang, Y. B.; Sun, X.; Cao, D. X.; Gao, G. H.; Yang, Z. Z.; Zhu, H. L.; Wang, Y. Self-stabilized $LiNi_{0.8}Mn_{0.1}Co_{0.1}O_2$ in thiophosphate-based all-solid-state batteries through extra LiOH. *Energy Storage Mater.* **2021**, *41*, 505–514.

[55] Pei, B.; Zhou, H.; Goel, A.; Zuba, M.; Liu, H.; Xin, F. X.; Whittingham, M. S. Al substitution for Mn during Co-precipitation boosts the electrochemical performance of $LiNi_{0.8}Mn_{0.1}Co_{0.1}O_2$. *J. Electrochem. Soc.* **2021**, *168*, 050532.

[56] Deng, S. X.; Li, X.; Ren, Z. H.; Li, W. H.; Luo, J.; Liang, J. W.; Liang, J. N.; Banis, M. N.; Li, M. S.; Zhao, Y. et al. Dual-functional interfaces for highly stable Ni-rich layered cathodes in sulfide all-solid-state batteries. *Energy Storage Mater.* **2020**, *27*, 117–123.

[57] Niu, C. Q.; Luo, W. J.; Dai, C. M.; Yu, C. B.; Xu, Y. X. High-voltage‐tolerant covalent organic framework electrolyte with holistically oriented channels for solid-state lithium metal batteries with nickel-rich cathodes. *Angew. Chem., Int. Edit.* **2021**, *60*, 24915–24923.

[58] Shrestha, S.; Kim, J.; Jeong, J.; Lee, H.; Kim, S. C.; Hah, H. J.; Oh, K.; Lee, S. Effect of amorphous LiPON coating on electrochemical performance of $LiNi_{0.8}Mn_{0.1}Co_{0.1}O_2$ (NMC811) in all solid-state batteries. *J. Electrochem. Soc.* **2021**, *168*, 060537.

[59] Ye, L. H.; Li, X. A dynamic stability design strategy for lithium metal solid state batteries. *Nature* **2021**, *593*, 218–222.

[60] Becke, A. D.; Edgecombe, K. E. A simple measure of electron localization in atomic and molecular systems. *J. Chem. Phys.* **1990**, *92*, 5397–5403.

[61] Yoon, M.; Dong, Y. H.; Hwang, J.; Sung, J.; Cha, H.; Ahn, K.; Huang, Y. M.; Kang, S. J.; Li, J.; Cho, J. Reactive boride infusion stabilizes Ni-rich cathodes for lithium-ion batteries. *Nat. Energy* **2021**, *6*, 362–371.